A stalactite record of four relative sea-level highstands during the Middle Pleistocene Transition

Paolo Stocchi, Fabrizio Antonioli, Paolo Montagna, Fabrizio Pepe, Valeria Lo Presti, Antonio Caruso, Marta Corradino, Gino Dardanelli, Pietro Renda, Norbert Frank, et al.

A stalactite record of four relative sea-level highstands during the Middle Pleistocene Transition

Paolo Stocchi[1,*], Fabrizio Antonioli[2], Paolo Montagna[3], Fabrizio Pepe[4], Valeria Lo Presti[2], Antonio Caruso[4], Marta Corradino[4], Gino Dardanelli[5], Pietro Renda[4], Norbert Frank[6], Eric Douville[7], François Thil[7] , Bas de Boer[8], Rosario Ruggieri[9,10], Rosanna Sciortino[5] and Catherine Pierre[11]

[1]NIOZ Royal Netherlands Institute for Sea Research, Department of Coastal Systems, and Utrecht University, Landsdiep 4, 1797 TA, Den Hoorn, Texel, the Netherlands

[2]ENEA National Agency for New Technologies, Energy and Environment, Via Anguillarese 301, 00060, S. Maria di Galeria, Rome, Italy

[3]ISMAR-CNR, Via Gobetti 101, 40129 Bologna, Italy

[4]Dipartimento di Scienze della Terra e del Mare, Via Archirafi, 22, Università di Palermo, Palermo, Italy

[5]Dipartimento di Ingegneria Civile, Ambientale, dei Materiali (DICAM), Università di Palermo, Viale delle Scienze, Ed. 8, 90128 Palermo, Italy

[6]Universität Heidelberg, Im Neuenheimer Feld 229, 69120 Heidelberg, Germany

[7]LSCE/IPSL, UMR 8212 CNRS-CEA-UVSQ, 91198, Gif-sur-Yvette, France

[8]IMAU, Utrecht University, Utrecht, The Netherlands

[9]CIRS Centro Ibleo di Ricerche Speleo-Idrogeologiche, Via Torrenuova 87, 97100, Ragusa, Italy

[10]University of Nova Gorica, SI-5000 Nova Gorica, Slovenia

[11]LOCEAN, Jussieu, Paris Cedex, France

[*]Corresponding author: Paolo.Stocchi@nioz.nl

Abstract

Ice-sheet and sea-level fluctuations during the Early and Middle Pleistocene are as yet poorly understood. A stalactite from a karst cave in North West Sicily (Italy) provides the first evidence of four marine inundations that correspond to relative sea-level (RSL) highstands at the time of the Middle Pleistocene Transition. The speleothem is located ~ 97 m above mean sea level (msl) as result of Quaternary uplift. Its section reveals three marine hiatuses and a coral overgrowth that fixes the age of the fourth and final marine ingression at 1.124 ± 0.2 million years ago, thus making this speleothem the oldest stalactite with marine hiatuses ever studied to date. Scleractinian coral species witness light-limited conditions and water depth of 20-50 m. Integrating the coral-constrained depth with the geologically constrained uplift rate and an ensemble of RSL scenarios, we find that the age of the last marine ingression most likely coincides with Marine Isotope Stage 35 on the basis of a probabilistic assessment. Our findings are consistent with a significant Antarctic ice-sheet retreat.

Keywords: Interglacial(s); Pleistocene; Sea Level changes; Paleogeography; Western Europe; Speleothems; Corals, Stable isotopes; U-Th dating; $^{87}Sr/^{86}Sr$ ages, Geomorphology, coastal

1. Introduction

Changes in solar radiation due to orbital forcing and variations in the concentrations of atmospheric greenhouse gases led to a succession of glacial and interglacial periods during the Pleistocene (Bintanja et al., 2005; De Boer et al., 2013; Rohling et al., 2014). Large fluctuations in ice volumes on both hemispheres resulted in significant sea-level changes that can be inferred from proxy records such as benthic and planktonic foraminiferal $\delta^{18}O$ from deep-sea sediment cores (Rohling et al., 2014; Lisiecki and Raymo, 2004; Grant et al., 2014). However, $\delta^{18}O$ time series lack direct age control and require numerical iteration to decouple the convolved deep-water temperature and global ice mass signal (Bintanja et al., 2005; De Boer et al., 2014). Relative sea-level (RSL) changes can be permanently

recorded by coastal geomorphological markers that are linked to coastal uplift (Ferranti et al., 2006; Antonioli et al., 2015). A common approach in constraining Pleistocene ice-sheet fluctuations is to date RSL markers such as shallow karst cave speleothems and measure their elevations with respect to modern mean sea level. The subaerial growth of speleothems inside caves that are connected to the sea is interrupted during marine floodings. Successive marine inundations appear as series of concentric hiatuses within speleothem sections and can be converted into RSL changes (Dutton et al., 2009; Richards et al., 1994). While paleo sea-level markers such as fossil beaches from the Pliocene have been identified worldwide (Rovere et al., 2014), speleothems that can be used as reliable RSL indicators that are older than 1 million years are extremely rare because of cliff retreat due to coastal erosion and active tectonics (Breitenbach et al., 2005; Artyushkov, 2012).

In this work we reconstruct the conditions and the chronology of the events that led to the occurrence and preservation of four marine ingressions that are recorded by a stalactite that is located inside the uplifted Rumena karst cave (RKC) in Custonaci, North West Sicily (NWS; Fig. 1, 2). The descriptive work of Ruggieri and De Waele (2014) provides information on the RKC morphology as well as a tentative minimum age of 1,200 ka for the cave based solely on the age of the corals encrustation as provided by Antonioli et al. (2012; 2014)

Here we adopt a multidisciplinary and quantitative approach by combining geodetic measurements, dating techniques, geological and paleoecological observations and reconstructed RSL curves that are based on proxy data and numerical modelling. We aim at pinpointing the elevation of the uplifting stalactite in time and with respect to the fluctuating sea level. Our main goal is to correlate the marine ingressions that are observed within the stalactite section to the RSL changes that characterize the proxy-based sea-level curves. We evaluate the bathymetric conditions during the last flooding event with respect to present-day local sea level.

2. Geological settings and Quaternary uplift rate

78 NWS is a segment of the Early Miocene to present-day Sicilian-Maghrebian Fold and Thrust Belt (Fig.
79 2). The latter consists of a thin-skinned, south-verging fold and thrust system formed by Mesozoic–
80 Tertiary carbonates, siliciclastic and evaporites, locally overlain by late orogenic clastic deposits
81 (Catalano et al., 2000). Quaternary extensional and strike-slip faults deformed the nappe pile and
82 formed structural ridges and intervening basins (Mauz et al., 1997). Post Middle-Pleistocene coastal
83 terraces are presently distributed around the NWS at elevations up to 160 m above modern mean sea
84 level (msl) (Di Maggio et al., 2009), thus demonstrating that vertical uplift occurred as a consequence
85 of deep-seated processes. A swarm of NW-SE and N-S/NNE-SSW trending faults accommodates the
86 structural separation between the Rocca Rumena Ridge, where the cave karst formed, and the
87 Castelluzzo and Cornino coastal plains (Fig. 2; Catalano et al., 2006). Close to Custonaci, eolian
88 deposits (Fig. 3a and b) and shallow marine depositional systems (Fig. 3c and d) are preserved above
89 Mesozoic-Paleogene carbonates at an elevation of 120±10 m above msl in close proximity to the RKC
90 (see Fig. 2; Di Maggio et al., 2009). Although index fossils in these deposits are lacking, based on
91 regional stratigraphic correlations, it has been proposed that they formed during the transgressive
92 depositional cycle of the Early Pleistocene Calabrian Stage, which comprises the Marine isotope Stages
93 (MIS) 53-35 (Ruggeri et al., 1979). The absolute age of 1.48 (± 0.10) Ma inferred for the oldest
94 deposits (Ruggeri et al., 1979) suggests a long-term linear uplift rate of 0.081±0.014 mm yr^{-1}. The latter
95 is consistent with a shorter-term estimate of ~ 0.08 mm yr^{-1} that is based on MIS 5e (~125,000 years
96 ago and assuming an elevation of ~6.0 m above msl paleo sea level) elevated coastal terraces that lie
97 approximately 1 km to the west at ~16 m above msl (Antonioli et al., 2002; Lambeck et al., 2004).
98
99 **3. Materials and Methods**
100 Here we describe our multidisciplinary approach that incorporates instrumental geodetic measurements
101 of the stalactite elevation, laboratory analytical dating techniques for the age of speleothem and fossil
102 corals and numerical modelling of RSL change.

3.1 Orthometric height of the stalactite

The orthometric height of the stalactite is the result of two integrated different geodetic surveying techniques: tacheometric and GNSS methods (Dardanelli et al., 2009). A static GNSS survey was conducted on several control points close to the RKC with the following acquisition parameters: 10 km baseline distance, observation time 4 hours for each point, cut-off angle 10 degrees and rate 5 seconds. The goal of the survey was the estimation of geoid undulation within the investigated zone. The data were calculated relative to the reference station TRAP (Trapani) of the UNIPA NRTK GNSS permanent GNSS network (Dardanelli et al., 2009); the geodetic undulation is approximately 43.52 m. A triple-difference analysis was performed by means of Network Deformation Analysis software package, which makes ionospheric and tropospheric corrections. The modelling of the tropospheric delay was carried out by using the ideal gas law refractivity model published by (Saastamoinen, 1972; Niell, 1996), while the modelling of ionospheric error was performed using the Total Electron Content (Klobuchar, 1996) with daily parameter values supplied by the Center for Orbit Determination in Europe of the Astronomical Observatory of the University of Bern. In addition, the ocean loading correction and the zenith troposphere delay estimation (which affects the baseline coordinates) were based on a hydrodynamic model (Schwiderski, 1980). We also performed a correction of antenna phase centre position using precise ephemeris. To fix the phase ambiguity, we used the LAMBDA method associated with a secondary test on the "ratio" (Teunnisen et al., 1995), inserting the parameters of rotation of the Earth (Earth Orientation Parameters) and the values of the ocean tides to obtain an accurate result. The difference in elevation between the stalactite and the known points was derived by means of tacheometric levelling. Using the backward intersection method, we connected the tacheometric survey inside the cave to the GNSS survey.

3.2 U/Th dating

Two small pieces of carbonate (~ 200 mg) were extracted from the innermost and outermost layers of the stalactite (Fig. 1f) using a diamond-studded blade. The fragments were mechanically cleaned using the diamond blade to remove any visible contamination, leached with 0.1 HCl and dissolved with diluted HCl. The solution was equilibrated with a mixed $^{236}U/ ^{233}U/ ^{229}Th$ spike, and the U and Th fractions were separated using UTEVA resin (Eichrom Technologies, USA). U and Th separation and purification followed a procedure slightly modified from Douville et al., (2010). Uranium and thorium isotopes were analysed using a ThermoScientific NeptunePlus MC-ICP-MS at the Laboratoire des Sciences du Climat et de l'Environnement in Gif-sur-Yvette. Mass bias was corrected using an exponential mass fractionation law (normalized to the natural $^{238}U/ ^{235}U$ isotopic ratio) and the standard/sample bracketing technique (using a mixture of our triple spike and HU-1). For more details on the analytical procedure see Pons-Branchu et al. (2014).

3.3 Strontium isotope analysis

Numerical ages of the encrusted corals (Fig. 1f) were estimated using Sr isotopes measured at the Laboratoire des Sciences du Climat et de l'Environnement in Gif-sur-Yvette (France). Three small coral fragments (3-5 mg) corresponding to the thecal walls were extracted from the outermost coral overgrowth (Fig. 1f) and carefully cleaned using a handheld dental drill bit in order to remove the external bioeroded zone, corresponding to ~ 400 μm. The internal portion was further polished upon removal of other visible contaminants. The sub-samples were examined using a binocular microscope to ensure against the presence of deep-penetrating and sediment-filled cavities and finally crushed into a powder with an agate mortar and pestle. The coral powder was rinsed three times with MilliQ water in acid-cleaned bullets before leaching with 0.3% acetic acid to remove 30-40% of $CaCO_3$. This first leaching step is designed to remove ions from exchangeable or leachable sites on the mineral surfaces. The remaining material was rinsed with MilliQ water and leached again with 0.4% acetic acid to remove 30% of the $CaCO_3$ for analysis, following the procedure published by Li et al. (2011). The

supernatant solutions were evaporated and adjusted to 3N HNO_3 for ion exchange chromatography. The solutions were loaded into 300 µl columns containing 100-150 µm bead size Eichrom Sr-SPEC resin to remove matrix and isolate Sr from other major and trace elements (e.g., the interfering elements Ca, Rb and REE). The columns were pre-flushed with 1 ml 3N HNO_3 and 3 ml MilliQ-water and conditioned using 1 ml 3N HNO_3 . Strontium was eluted from the columns with 2.5 ml MilliQ-water, and each solution was adjusted to 0.5 N HNO_3 for isotopic measurements. A chemical blank was also prepared, following identical procedural steps. Strontium isotope ratios were measured using a multicollector-ICPMS ThermoScientific Neptune Plus. All the solutions were diluted to 50 ppb of Sr and introduced into the Neptune using an ESI-APEX desolvating system and a 100 µl/min nebulizer. The sensitivity of the 50 ppb Sr solution was approximately 8 V at the ^{88}Sr peak, and the chemical blank level was 0.008 V. The samples and standards were analysed in a static multi-collection mode in a single block of 50 cycles with an integration time of 8 seconds per cycle. The instrumental mass fractionation was corrected for by using a stable isotopic $^{86}Sr/^{88}Sr$ ratio of 0.1194 and an exponential law. No isobaric corrections for Ca dimers and argides were required, and only minor corrections for ^{87}Rb to ^{87}Sr were considered. A correction was also applied for krypton isobaric interferences. Repeated measurements of strontium isotope standard NBS-987 during the analytical session yielded a mean $^{87}Sr/^{86}Sr$ value of 0.710264 ± 0.000014 (2σ SD, n = 11, corresponding to an external reproducibility of 20 ppm). The $^{87}Sr/^{86}Sr$ ratio for all the samples was corrected for instrumental bias to an accepted value for NBS-987 of 0.710248 (McArthur et al., 2001). All the $^{87}Sr/^{86}Sr$ ratios were converted into numerical ages using the regression curves LOWESS look-up Table version 4: 08/04 (revised from Li et al., 2011; see Table 1). The total uncertainty in $^{87}Sr/^{86}Sr$ (±0.000014) was calculated by adding in quadrature the analytical uncertainty on the standard measurement (2σ SD = ±0.000014) to the uncertainty of the LOWESS curve for the period considered (0-2 Ma = ±0.000003), as suggested in equation 7.1 from McArthur et al., (2012). The lower and upper bounds on the ages were calculated based on the total $^{87}Sr/^{86}Sr$ uncertainty (Table 1).

178

179 **3.4 Reconstructed RSL curves**

180 Three independent RSL change scenarios are considered for the time interval between 0.9 and 1.5 Ma.
181 The RSL-ANICE scenario consists of an ensemble of RSL curves that are based on the ANICE global
182 ice-sheet chronology (De Boer et al., 2014). The predicted RSL curves account for local Glacial
183 Isostatic Adjustment (GIA) and result from the solution of the gravitationally self-consistent sea level
184 equation (SLE; Farrell and Clark, 1976) for a suite of mantle viscosity profiles. We solve the SLE by
185 means of the pseudo-spectral method (Mitrovica and Milne, 2003) with SELEN Fortran 90 code
186 (Spada and Stocchi, 2007). The solid Earth response to ice-sheet fluctuations is accounted for by a
187 spherical, self-gravitating, rotating, radially stratified, deformable but incompressible Maxwell
188 viscoelastic Earth rheological model (Mitrovica and Milne, 2003; Spada and Stocchi, 2007). We keep
189 the elastic lithosphere thickness fixed to 100 km. We vary the upper and lower mantle viscosity values
190 between 0.25 to 1.0 x 10^{21} and 2 to 10 x 10^{21} Pa·s, respectively, and generate a combination of 20
191 different mantle viscosity profiles. The second input of the SLE is the forcing function, which
192 represents the continental ice-sheet fluctuations through time. We employ two versions of the 2.2
193 million years long ice-sheet chronology that is described by ANICE ice-sheet model (De Boer et al.,
194 2014). The first version does include the contribution of summer austral insolation (SAI) to the
195 Antarctic Ice Sheet (AIS) variability (see AIS-SAI in Fig. 4), while in the second version of ANICE the
196 SAI is not accounted for (see AIS-NSAI in Fig. 4). Including SAI results in significant retreats of AIS
197 during the interglacials that characterize the MPT (Fig. 4). We solve the SLE for 40 models (20
198 viscosity profiles x 2 ANICE versions) and compute the RSL curves at the location of the speleothem
199 (red curve in Fig. 5a). The second RSL scenario (RSL-Rohling14) is based on the RSL curve for
200 Gibraltar that was derived by Rohling et al. (2014) through statistical analysis of previously published
201 proxy data from Wang et al. (2010; green curve in Fig. 5a). The third scenario (RSL-Elderfield12) is
202 complementary to RSL-Rohling14 and is based on proxy data from Elderfield et al. (2012; green curve

in Fig. 5a). Both proxy-based curves are corrected for the differential GIA response.

The average RSL change in time and its standard deviation are evaluated for all three RSL scenarios. These values are then used to randomly generate, by means of a Monte Carlo method, a normal distribution of RSL values in time. The same is done for the reconstructed elevation of the speleothem (based on linear interpolation). The four normal distributions are then overimposed to evaluate the probability (in time) for the speleothem to be intercepted by sea level and, consequently, to be located at a certain depth with respect to sea level.

4. Results

On the basis of the method described in Section 3.1, we estimate the orthometric height of the stalactite to be 97.12 m. By shifting the current elevation of the speleothem back in time according to the linear uplift rate of 0.081±0.014 mm yr^{-1} (see Section 2) and assuming that sea level has remained constant through time, an interception with current msl occurs at ~ 1.225 Ma (Fig. 5a). Both calculated U/Th ages for the spelean carbonate layers are beyond the upper limit of the ^{230}Th age range, indicating an age older than ~ 0.6 Ma (Cheng et al., 2013). The age of the stalactite is indirectly determined by analysing the coral overgrowth using the strontium isotope dating method (see Section 3.3). The $^{87}Sr/^{86}Sr$-derived ages of the three coral fragments encrusting the external surface of the speleothem are identical within error (Table 1), suggesting that the coral portions, which were carefully selected from the internal part of the thecal walls, were most likely pristine, and the ages can be considered reliable. Averaging the values of the three fragments yields a mean age for the corals of 1.124 ± 0.2 Ma, which represents the age of the last marine ingression. The calculated standard deviation corresponds to 2σ SD of the mean age. The latter broadly agrees with the age of interception between the speleothem and current msl.

The predicted RSL-ANICE ensemble is characterized by lower amplitude RSL fluctuations with respect to the proxy-based scenarios (Fig. 5a). In particular, the predicted RSL highstands during the

interglacial periods are significantly lower. Maximum RSL elevations of 4-6 m above current msl are found for MIS 25, 31 and 37 and only for GIA solutions that account for the combination of the AIS sensitivity to austral summer insolation (see AIS-SAI in Fig. 4) and a high viscosity contrast between the upper and lower mantle.

When the three RSL scenarios are adopted, different numbers and timings of intersections between the uplifting stalactite and sea level occur at different elevations above current msl (Fig. 5a). The age and elevation of old shallow marine deposits, together with the age of the coral overgrowth and the number of hiatuses within the stalactite, are necessary constraints to reconstruct the chronology of marine inundations. In particular, the permissible living depth range for the corals is fundamental to pinpoint the elevation of the stalactite with respect to sea level during the fourth marine ingression. Of the coral species that have been identified, *Cladopsammia rolandi* indicates a water depth ≥ 20 m, with specimens capable of surviving at depths ≥ 50 m under normal light conditions (Rosso et al., 2015; ZIbrowius, 1978). A water column height of 20 m above the stalactite is assumed as the minimum limit for the RSL peak height during the formation of the coral. Accordingly, we use a Monte Carlo approach to generate normal distributions around the mean values of, respectively, the elevation of the stalactite through time and the three RSL scenarios (Fig. 5a). We evaluate the probability in time that the reconstructed RSL was at least 20 m above the predicted elevation of the cave within the plausible age range for the formation of the coral. We find that the RSL-ANICE ensemble is able to satisfy the minimum depth requirement during the fourth marine ingression with very low probabilities, ~15% and ~10% for MIS 37 and 41, respectively (see Fig. 5b). Solutions for RSL-Rohling14 indicate MIS 37 and 35 as the most likely events, with probabilities of 65% and 35%, respectively (see Fig. 5b). The same occurs for RSL-Elderfield12 scenarios, with the largest probability (100%) achieved for MIS 37, followed by MIS 35 (85%), MIS 39 (60%) and MIS 41 (65%) (see Fig. 5b).

5. Discussion

253 The requirement of a maximum of three interceptions before the formation of the coral encrustation
254 restricts the range of plausible solutions and shifts the chronological sequence of events to before the
255 MIS 31 interglacial. Although MIS 37 is the most likely event for each of the three scenarios (Fig. 5b),
256 the occurrence of a comparable RSL peak immediately afterwards suggests that the formation of the
257 corals occurred during MIS 35, which is also closer in time to the mean age of the corals. The RSL
258 highstands that follow MIS 35 are characterized by lower amplitudes. According to the RSL-Rohling14
259 and RSL-Elderfield12 scenarios, two interceptions between the stalactite and sea level might have
260 occurred after MIS 35 and before MIS 23. However, these would have resulted in lower highstands that
261 could not have interfered with previous coral encrustations. After MIS 25 the transition towards non-
262 linear responses of ice sheet to astronomical and climatological parameters resulted in long-period
263 glaciations that, together with the uplift, prevented further marine inundation of the RKC.
264 The local sea level during the MIS 35 interglacial was 20-30 m higher than present, which suggests that
265 a significant retreat of the West and East Antarctic Ice Sheet (WAIS and EAIS, respectively) occurred.
266 The ANICE ice-sheet model reconstruction does not show a significant retreat of the AIS because the
267 ice-sheet reconstruction is largely driven by the smoothed $\delta^{18}O$ stack curve (Lisiecki and Raymo,
268 2005), whereas regional RSL records might show more amplified variability (De Boer et al., 2014;
269 Konijnendijk et al., 2016). A marine transgression during MIS 35 was reported in form of a change in
270 mollusks species recorded by sediments in the slowly uplifting northern Po Plain (Gianolla et al.,
271 2010). This correlates to an RSL highstand that was observed for the same region by Scardia et al.
272 (2006). Deep-sea sediment cores from two drilling sites off East Antarctica (Prydz Bay and South
273 Atlantic), however, show that ice-rafted debris was still being produced during MIS 35 (Teitler et al.,
274 2015). This implies that there was an active sector of the EAIS that was capable of launching icebergs
275 into the Southern Ocean. Only later, between MIS 33 and 31, did a widespread retreat of AIS, with
276 increased contributions from EAIS, occur, resulting in an abrupt change in sedimentation. We argue,
277 therefore, that the drilling sites studied by Teitler et al. (2016) might have been mostly sensitive to the

278 northeastern portion only of the EAIS, which was still active during the MIS 35 interglacial. The far-
279 field site of Custonaci, instead, recorded the cumulative response of local sea level to the retreat of
280 WAIS and southern portions of EAIS.
281
282 **6. Conclusions**
283 The RKC speleothem section is the oldest stalactite containing marine hiatuses ever studied to date and
284 is the first direct geological evidence of RSL changes during the MPT. The formation and subsequent
285 preservation of the three hiatuses and of the corals encrustation are direct consequences of two
286 independent processes that worked in opposite direction. Quaternary uplift, which is a reflection of
287 deep-seated geodynamic processes, first facilitated marine ingressions by elevating the RKC towards
288 msl. During this time, higher-frequency RSL fluctuations left permanent marks in the speleothem,
289 which was very close to current msl. The transition from 41,000 to 100,000 periodicity in RSL
290 fluctuations contributed to the permanent disconnection of the uplifting cave with msl and prevented
291 any further inundation. The corals encrustations, which mark the last marine ingression, show that local
292 sea level rose up to 20-30 m above present. This implies that among the several factors that contributed
293 to local RSL rise, a significant AIS retreat likely occurred. Our results, combined with coeval AIS-
294 proximal sedimentological observations, confirm that the variability of AIS during climate transitions
295 is sectoral (Teitler et al., 2015). The evidence presented in this study agrees with predictions for both
296 the past and near future of AIS response to climate variability and show that different portions of EAIS
297 likely contribute to sea-level highstands during warm periods (Pollard and De Conto, 2009; Dutton et
298 al., 2015).
299
300
301
302

References and Notes:

Antonioli, F., Cremona, G., Immordino, F., Puglisi, C., Romagnoli, C., Silenzi, S., Valpreda, E., and Verrubbi, V., 2002, New data on the Holocenic sea-level rise in NW Sicily (Central Mediterranean Sea): Global and Planetary Change, v. 34, p. 121-140.

Antonioli, F., Montagna, P., Caruso, A., Ruggieri, R., Lo Presti, V., Silenzi, S., Frank, N., Douville, E. and C. Pierre, 2012, Investigation of marine and continental layers in a stalactite older than 1 million years (Custonaci, north-western sector of Sicily), SLALOM 2012, abstract volume, Athens 19–22 March 2012, p. 57–58.

Antonioli, F., Ruggieri, R., Montagna, P., Pepe, F., Caruso, A., Stocchi, P., Renda, P., Lo Presti, V., Frank, N., Douville, E., Pierre, C., Messina Panfalone, D., 2014, The geosite Rumena cave a unique paleoclimate and sea level archive in the Mediterranean area (northwestern Sicily). 4th International Symposium, Karst Geosites, abstract volume, Favignana 30 May – 2 June, p. 64–66.

Antonioli, F., Lo Presti, V., Rovere, A., Ferranti, L., Anzidei, M., Furlani, S., Mastronuzzi, G., Orru, P.E., Scicchitano, G., and Sannino, G., 2015. Tidal Notches in Mediterranean Sea: a comprehensive analysis. Quaternary Science Reviews, 119, 66-84.

Artyushkov, E.V., 2012, Vertical crustal movements on the continents as a reflection of deep-seated processes in the earth's crust and mantle: Geological effects. Herald of the Russian Academy of Sciences, v. 82, no. 6, p. 432-446.

Bintanja, R., Van de Wal, R.S.W., and Oerlemans, J., 2005, Modelled atmospheric temperatures and global sea level over the past million years: Nature, v. 437, p. 125-128.

Breitenbach, S., Fernandez, D., Adkins, J., Mingram, B., Oberhänsli, H., and Haug, G., 2005, Speleothem records older than 500 ka from Southern Siberia: Proc. 14th International

Conference of Speleology, Athens 2005, p. 1-7.

Catalano, R., Franchino, A., Merlino, S., and Sulli, A., 2000, Central western Sicily structural setting interpreted from seismic reflection profiles: Mem. Soc. Geol. It., v. 55, p. 5-16.

Catalano, R., Abate, B., Agate, M., Basilone, L., Di Maggio, C., Di Maio, D., Mancuso, M., Sulli, A., Vaccaro, F., Arnone, M., Avellone, G., Barchi, M., Bonomo, S., Cottone, S., D'Argenio, A., Fallo, L., Lo Cicero, G., Lo Iacono, C., Lucido, M., Pepe, F., Scannavino, M., and Sprovieri, R., 2006, Carta geologica d'Italia alla scala 1:50.000 del foglio 593 "Castellammare del Golfo": Progetto CARG, p. 1.

Cheng, H., Edwards, R.L., Shen, C.-C., Polyak, V.J., Asmeron, Y., Woodhead, J., Hellstrom, J., Wang, Y., Kong, X., Spötl, C., Wang, X., Alexander Jr., E.C., 2013, Improvemetns in ^{230}Th dating, ^{230}Th and ^{234}U half-life values, and U/Th isotopic measurements by multi-collector inductively coupled plasma mass spectrometry. Earth and Planetary Science Letters, v. 371-372, p. 82–91.

Clark, P.U., and Pollard, D., 1998, Origin of the middle Pleistocene transition by ice sheet erosion of regolith: Paleoceanography, v. 13, no. 1, p. 1-9.

Dardanelli, G., Franco, V., Lo Brutto, M., 2009, Accuracy and reliability in GNSS NRTK, Proceedings of European Navigation Conference - Global Navigation Satellite Systems, Naples, Italy.

De Boer, B., Van de Wal, R.S.W., Lourens, L.J., and Bintanja, R., 2013, A continuous simulation of global ice volume over the past 1 million years with 3-D ice-sheet models: Climate Dynamics, v. 41, p. 1365-1384.

De Boer, B., Lourens, L.J., and Van de Wal, R.S.W., 2014, Persistent 400,000-year variability of Antarctic ice volume and the carbon cycle is revealed throughout the Plio-Pleistocene: Nature Communications, v. 5:2999, doi:10.1038/ncomms3999.

Di Maggio, C., Agate, M., Contino, A., Basilone, L., Catalano, R., 2009. Unconformity-bounded stratigraphic units of Quaternary deposits mapped for the CARG Project in Northern and Western Sicily: Alpine and Mediterranean Quaternary, v. 22, 2, 354-364.

352 Douville E., Salle E., Frank N., Eisele M., Pons-Branchu E., Ayrault S., 2010, Rapid and accurate U-
353 Th dating of ancient carbonates using inductively coupled plasma-quadrupole mass
354 spectrometry: Chemical Geology 272, 1-11.
355 Dutton A., Antonioli F., Bard E., M. Esat T., Lambeck K, McCulloch M., 2009. Phasing and amplitude
356 of sea level and climate change during the penultimate interglacial. Nature Geosciences, 355-
357 359.
358 Dutton, A., Carlson, A.E., Long, A.J., Milne, G.A., Clark, P.U., DeConto, R., Horton, B.P., Rahmstorf,
359 S., and Raymo, M.E., 2015. Sea-level rise due to polar ice-sheet mass loss during past warm
360 periods. Science, v. 349, doi:10.1126/science.aaa4019.
361 Elderfield, H. et al., 2012, Evolution of ocean temperature and ice volume through the Mid-Pleistocene
362 Climate Transition. Science 337, 704–709.
363 Farrell, W.E., and Clark, J.A., 1976, On postglacial sea level: Geophys. J.R. Astron. Soc., v. 46, p.
364 647-667.
365 Ferranti, L., Antonioli, F., Mauz, B., Amorosi, A., Dai Pra, G., Mastronuzzi, G., Monaco, C., Orrù, P.,
366 Pappalardo, M., Radtke, U., Renda, P., Romano, P., Sansò, P., Verrubbi, V., 2006. Markers of
367 the last interglacial sea-level high stand along the coast of Italy: tectonic implications.
368 Quaternary International 145-146, 30–54.
369 Gianolla, D., Negri, M., Basso, D., and Sciunnach, D., 2010. Malacological response to Pleistocene
370 sea-level change in the northern Po Plain, N. Italy: detailed palaeoenvironmental
371 reconstructions from two lombardian cores. Rivista Italiana di Paleontologia e Stratigrafia, vol.
372 116, no. 1, pp. 79-102.
373 Grant, K.M., Rohling, E.J., Bronk Ramsey, C., Cheng, H., Edwards, R.L., Florindo, F., Heslop, D.,
374 Marra, F., Roberts, A.P., Tamisiea, M.E., &and Williams, F., 2014, Sea-level variability overt
375 five glacial cycles: Nature Communications, doi:10.1038/ncomms6076.
376 Klobuchar, J. A., 1996, Global Positioning System: Theory and Applications. Volume I, Cap. XII:

Ionospheric effects on GPS, pp. 485-515, American Institute of Aeronautics and Astronauitcs Inc.

Konijnendijk, T.Y.M., Ziegler, M., and Lourens, L.J., 2016. On the timing and forcing mechanisms of late Pleistocene glacial terminations: Insights from a new high-resolution benthic stable oxygen isotope record of the eastern Mediterranean, Quaternary Science Reviews, 129, 308-320, doi: 10.1016/j.quascirev.2015.10.005.

Kopp, R.E., Simons, F.J., Mitrovica, J.X., Maloof, A.C., and Oppenheimer, M., 2009, Probabilistic assessment of sea level during the last interglacial stage: Nature, v. 462, p. 863-868.

Lambeck, K., Antonioli, F., Purcell, A., and Silenzi. S., 2004, Sea level change along the Italian coast for the past 10,000 years: Quaternary Science Reviews, v. 23, p. 1567-1598.

Li D., Shields-Zhou G.A., Ling H.F., Thirlwall M. (2011). Dissolution methods for strontium isotope stratigraphy: Guidelines for the use of bulk carbonate and phosphorite rocks. Chemical Geology 290, 133-144.

Lisiecki, L., and Raymo, M., 2005, A Pliocene-Pleistocene stack of 57 globally distributed benthic $\delta^{18}O$ records: Paleoceanography, v. 20, PA1003, doi:10.1029/2004PA001071.

Mauz, B., Buccheri, G., Zoller L., and Greco, A., 1997, Middle to upper Pleistocene morphostructural evolution of the NW coast of Sicily: thermoluminescence dating and paleontological stratigraphical evaluations of littoral deposits: Palaeogeogr. Palaeoecol. Palaeogeogr., v. 128, p. 269-285.

McArthur J.M., Howarth R.J. and Bailey T.R. (2001) Strontium Isotope Stratigraphy: LOWESS Version 3: Best Fit to theMarine Sr-Isotope Curve for 0–509 Ma and Accompanying Look-up Table for Deriving Numerical Age, The Journal of Geology, 109, 155–170.

McArthur J.M., Howarth R.J. and Shields G.A. (2012) Strontium Isotope Stratigraphy. In Gradstein F., Ogg. J., Schmitz M. and Ogg G. (Eds), The Geologic Time Scale 2012, ed. Elsevier, 127-144.

Mitrovica, J.X., and Milne, G.A., 2003, On post-glacial sea level: I. General theory. Geophys. J. Int., v.

154, p. 253-267.

Niell, A. E, 1996, Global mapping functions for the atmosphere delay at radio wavelengths. Journal of Geophysical Research, vol. 100, n. B2:3227-3246.

Pollard, D. and Deconto, R.M., 2009. Modelling West Antarctic ice sheet growth and collapse through the past five million years. Nature, v. 458, p. 329-333.

Pons-Branchu E., Douville E., Roy-Barman M., Dumont E., Branchu P., Thil F., Frank N., Bordier L., Borst W. (2014) A geochemical perspective on Parisian urban history based on U-Th dating, laminae counting and yttrium and REE concentrations of recent carbonates in underground aqueducts. Quaternary Geochronology 24, 44-53.

Richards D.A., Smart P.L., Edwards R.L., 1994, Maximum sea levels for the last glacial period from U-series ages of submerged speleothems, Nature 367, 357-360.

Rohling, E.J., Foster, G.L., Grant, K.M., Marino, G., Roberts, A.P., Tamisiea, M.E., and Williams, F., 2014, Sea-level and deep-sea-temperature variability over the past 5.3 million years: Nature, v. 508, p. 477-482, doi:10.1038/nature13230.

Rovere, A., Raymo, M.E., Mitrovica, J.X., Hearthy, P.J., O'Leary, M.J., and Inglis, J.D., 2014. The Mid-Pliocene sea-level conundrum: Glacial isostasy, eustasy and dynamic topography. Earth and Planetary Science Letters, 387, 27-33.

Rosso, A., Sanfilippo, R., Ruggieri, R., Maniscalco, R., and Vertino, A., 2015, Exceptional record of submarine cave communities from the Pleistocene of Sicily (Italy): Lethaia, v. 48, p. 133-144.

Ruggeri, G., Sprovieri, R., and Unti M., 1979, Evidenze della trasgressione dell'Emiliano (Pleistocene inferiore) nella Sicilia Orientale: Boll. Soc. Geol. It., v. 98, p. 469-473.

Ruggieri, R., and De Waele, J., 2014. Lower- to Middle Pleistocene flank margin caves at Custonaci (Trapany, NW Sicily) and their relation with past sea levels. Acta Carsologica, 43/1, 11–22.

Saastamoinen, J., 1972, Atmospheric correction for the troposphere and stratosphere in radio ranging of satellites, Geophys. Monogr., 15, American Geophysical Union, Washington DC.

Scardia, G., Muttoni, G., and Sciunnach, D., 2006, Subsurface magnetostratigraphy of Pleistocene sediments from the Po Plain (Italy): Constraints on rates of sedimentation and rock uplift. GSA Bulletin, v. 118; no. 11/12; p. 1299–1312; doi: 10.1130/B25869.1.

Schwiderski, E. W., 1980, On charting global ocean tides, Reviews of Geophysics and Space Physics, 18, 243-268.

Spada, G., and Stocchi, P., 2007, SELEN: A Fortran 90 program for solving the ”sea-level equation”: Computers & Geosciences, v. 33, p. 538-562.

Teitler, L., Florindo, F., Warnke, D.A., Filippelli, G.M., Kupp, G., and Taylor, B., 2015, Antarctic Ice Sheet response to a long warm interval across Marine Isotope Stage 31: A cross-latitudinal study of iceberg-rafted debris: Earth and Planetary Science Letters, v. 409, p. 109-119.

Teunnisen, P. J. G., de Longe, P. J., Tiberius, C. C. J. M., 1995, The LAMBDA-method for fast GPS surveying. In: International Symposium “GPS Technology Applications” Bucharest, Romania.

Wang, P., Tian, J., and Lourens, L. J., 2010, Obscuring of long eccentricity cyclicity in Pleistocene oceanic carbon isotope records. Earth Planet. Sci. Lett. 290, 319–330.

Zibrowius, H., 1978, Les Scleractiniaires des grotte sous-marine en Mediterranee et dans l’Atlantique nord-orientale (Portugal,Madere, Canaries, Azores). Pubblicazioni della Stazione Zoologica di Napoli 40, 516 545.25.

Acknowledgments: We are thankful to David Richards, Christian Ohneiser and Enrico Di Stefano for their helpful comments. This work was partly financially supported by the grant “Fondo Finalizzato alla Ricerca 2012/2013 (CUP B71J12001450001)” funded by the University of Palermo (Italy).

FIGURE CAPTIONS

Figure 1. Study area (a) and details of the RKC (b-d). The cave wall (e) and the stalactite are covered by a coral encrustation. The stalactite section (f) reveals three concentric hiatuses. Lithophaga-produced boring holes penetrate the third hiatus. The external surface of the stalactite is covered by coral encrustations. The geographical coordinates of the RKC are 38.07 N and 12.66 E (UTM WGS84).

Figure 2. Simplified geological map of the study area in the North West Sicily (map adapted from the 1:50.000 Geological Map at a scale 1:50.000 (CARG Project; Catalano et al., 2006).

Figure 3. Thin Sections A and B – (samples Cu 13.1 and Cu 13.4) Photos of the eolian sandstones (qz - quartz; IO - iron oxide). C and D – (samples Cu 13.10a and Cu 13.10b.) Photos of calcarenites rich in foraminifera (El, Elphidium sp.; Gr – Globigerinoides ruber; Ec – Echinoid spine). Sites samples are indicated in Fig. S1.

Figure 4. Antarctic Ice Sheet (AIS) and Greenand Ice Sheet (GIS) ice volumes (expressed in meters of eustatic sea-level change) according to ANICE (22). Neglecting SAI results in a larger-than-today AIS during the interglacials that punctuate the MPT (solid red curve, AIS-NSAI). Accounting for SAI, instead, triggers significant retreats that result in eustatic sea-level highstands above present-day msl (AIS-SAI; ~5.5 m at MIS 31, ~4 m at MIS 25, ~2m at MIS 37). For both scenarios, the GIS is slightly larger than today (~ 1 m esl) and is also quite stable throughout the period under considerations.

Figure 5. (a) Elevation of the RKC in time (mean and standard deviation; dotted blue lines) with respect to three rsl change scenarios (95% confidence interval): RSL-ANICE (red shading), RSL-Rohling14 (blue shading), RSL-Elderfield12 (grey shading). The horizontal double-headed arrow indicates the age interval for the formation of the coral encrustation. (b) Probability of a water column height $\geq$ 20 m above the corals according to the three rsl change scenarios. The probability decreases with time as a consequence of the uplift of the RKC and long-term rsl drop (with decreasing amplitude of shorter-term fluctuations).

Figure 1

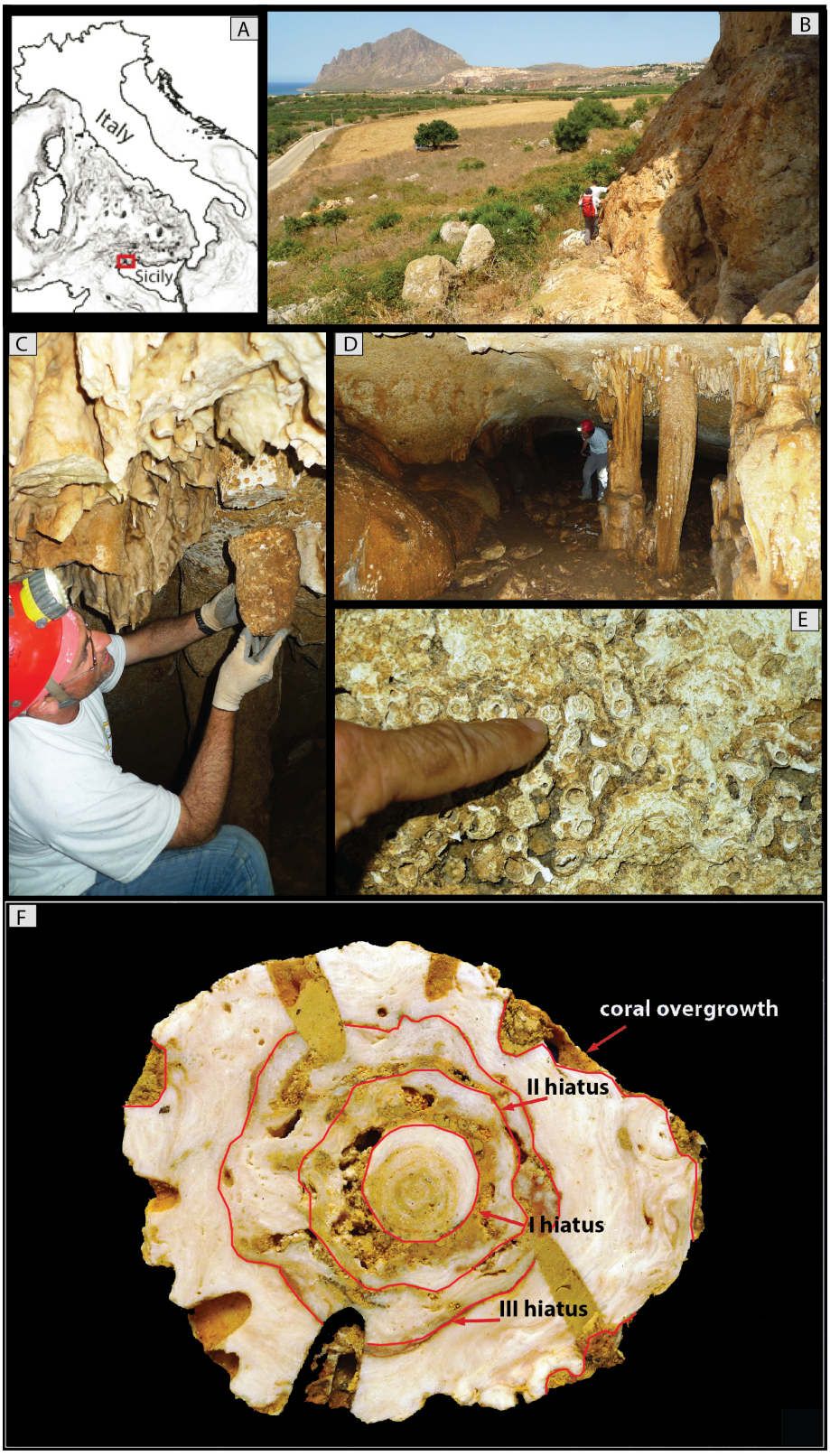
A
Italy
Sicily
B
C
D
E
F
coral overgrowth
II hiatus
I hiatus
III hiatus

Figure 2

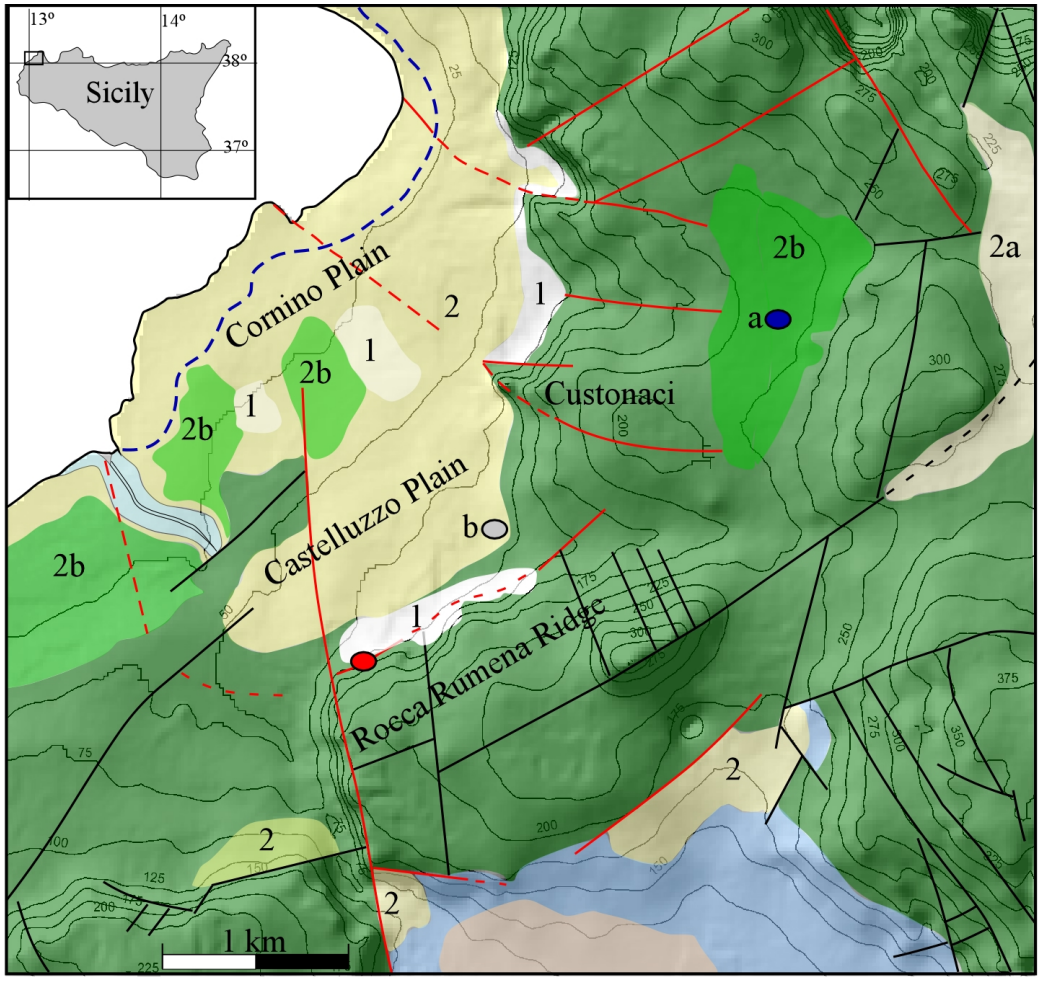

Rumena karst cave

Last Interglacial inner margin

Strike-slip fault

fault

Sites samples

a Aeolian sandstones (A and B in Fig. S2)

b Calcarenites rich in foraminifera (C and D in Fig. S2)

1 Debris

2a 2b 2 Bioclastic calcarenites and conglomerates (2), silt sand and gravel (2a), aeolian quartz-sand, paleosoils and colluvium (2b). Early Pleistocene

Biocalcarenites, biocalcirudites with fragments of lamellibranches, clays with intercalated sand and sandstone layers with local lens of send quartz and conglomerates. Early Miocene-middle Tortonian

Clays, sands, sandstones, quarzarenites and conglomerates. Terravecchia Formation. Late Tortonian-Early Messinian

Mesozoic-Paleogene carbonates

Figure 3

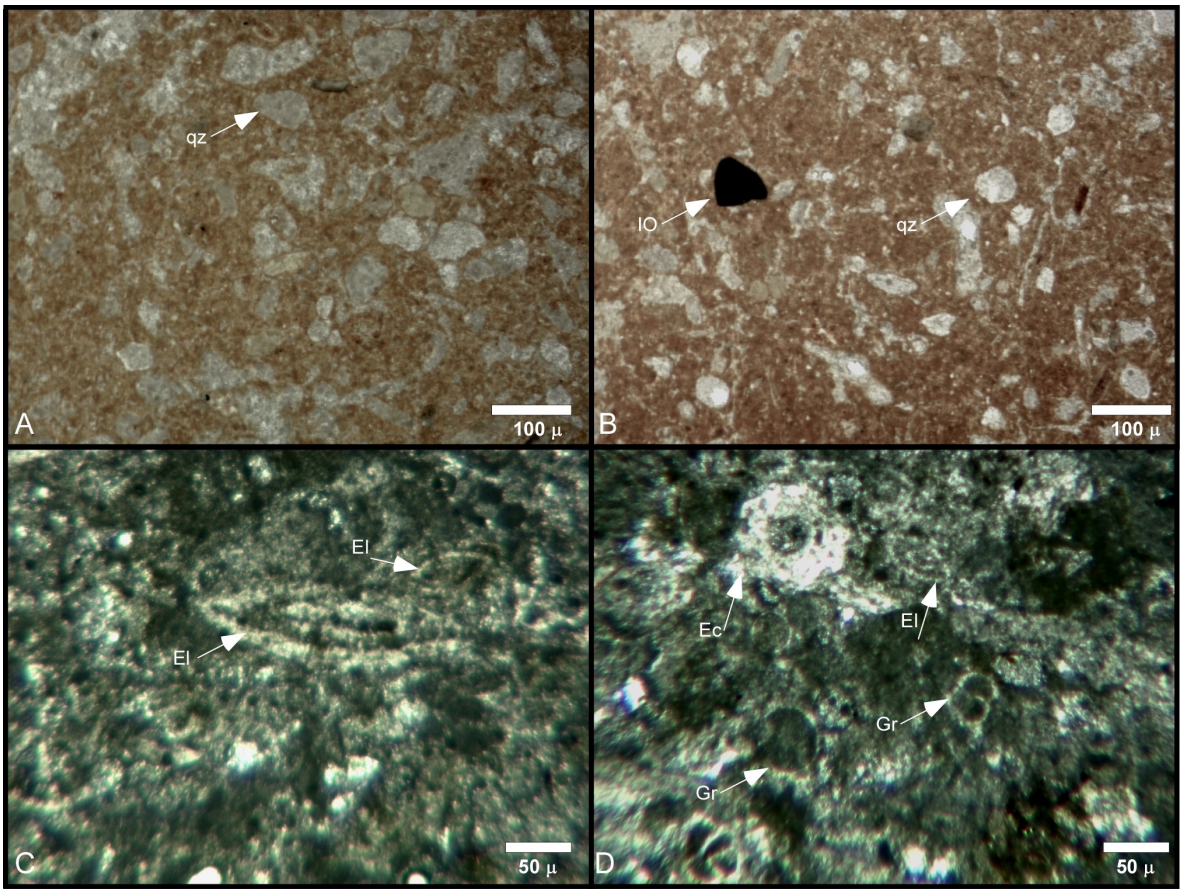

Figure 4

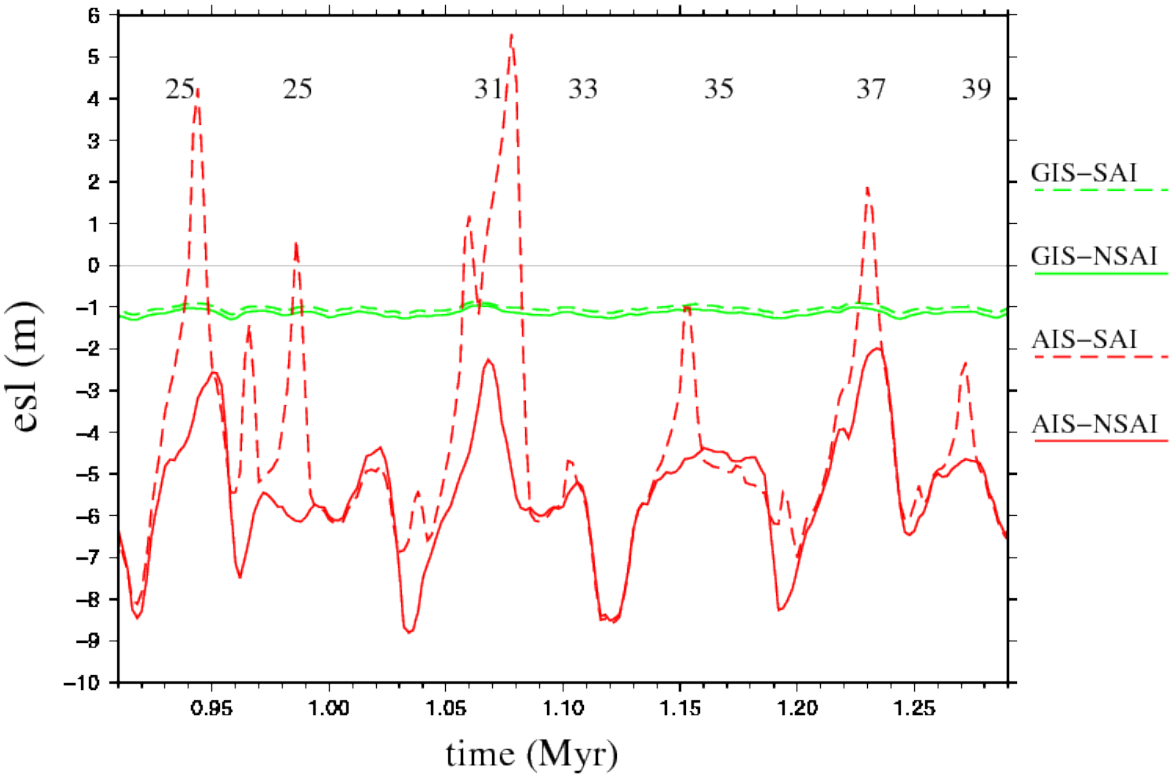
esl (m)
time (Myr)
25
25
31
33
35
37
39
GIS–SAI
GIS–NSAI
AIS–SAI
AIS–NSAI

Figure 5

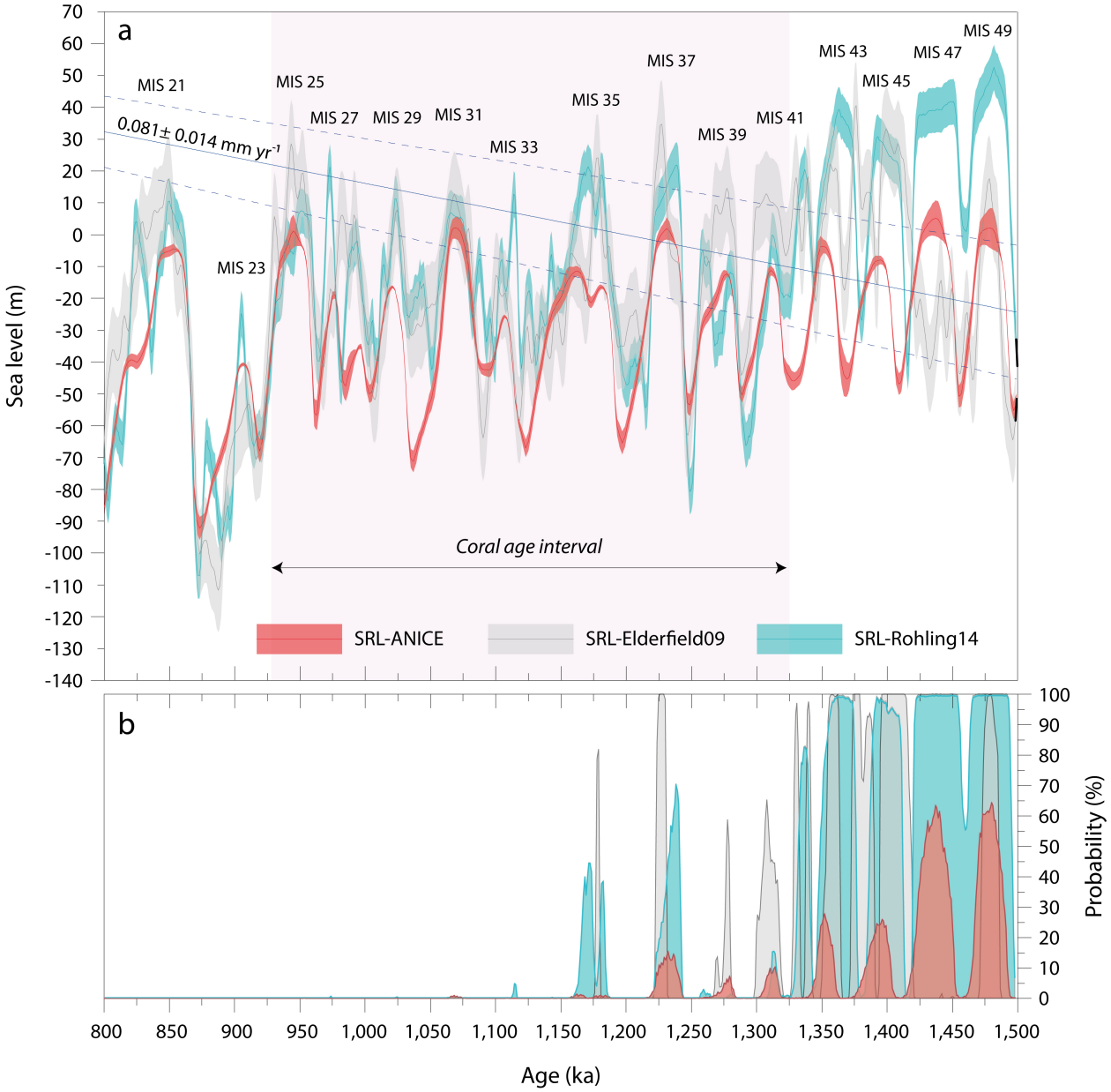
a
b
MIS 21
MIS 23
MIS 25
MIS 27
MIS 29
MIS 31
MIS 33
MIS 35
MIS 37
MIS 39
MIS 41
MIS 43
MIS 45
MIS 47
MIS 49
0.081± 0.014 mm yr-1
Coral age interval
SRL-ANICE
SRL-Elderfield09
SRL-Rohling14
Sea level (m)
Probability (%)
Age (ka)

568
569
570
571
572
573 **TABLES**

574 **Table 1.** $^{87}Sr/^{86}Sr$ ages (Ma) of the corals encrusting the stalactite.

Sample ID	Material	Method	$^{87}Sr/^{86}Sr$	Lower Age (Ma)	Mean Age (Ma)	Upper Age (Ma)
-2572-	Coral	MC-ICP-MS	0.709130 (14)	0.814	1.131	1.288
-2573-	Coral	MC-ICP-MS	0.709137 (14)	0.665	1.023	1.268
-2574-	Coral	MC-ICP-MS	0.709124 (14)	0.957	1.218	1.460
Mean value					**1.124**	
2 SD					**0.2**	

575